

# Nanoscale

Accepted Manuscript



This is an *Accepted Manuscript*, which has been through the Royal Society of Chemistry peer review process and has been accepted for publication.

*Accepted Manuscripts* are published online shortly after acceptance, before technical editing, formatting and proof reading. Using this free service, authors can make their results available to the community, in citable form, before we publish the edited article. We will replace this *Accepted Manuscript* with the edited and formatted *Advance Article* as soon as it is available.

You can find more information about *Accepted Manuscripts* in the [Information for Authors](#).

Please note that technical editing may introduce minor changes to the text and/or graphics, which may alter content. The journal's standard [Terms & Conditions](#) and the [Ethical guidelines](#) still apply. In no event shall the Royal Society of Chemistry be held responsible for any errors or omissions in this *Accepted Manuscript* or any consequences arising from the use of any information it contains.



## Nanoscale

## ARTICLE

## Designing Nanobowl Arrays of Mesoporous TiO<sub>2</sub> as an Alternative Electron Transporting Layer for Carbon Cathode-based Perovskite Solar Cells

Received 00th January 20xx,  
Accepted 00th January 20xx

DOI: 10.1039/x0xx00000x

www.rsc.org/

Xiaoli Zheng,<sup>1,a</sup> Zhanhua Wei,<sup>1,a</sup> Haining Chen,<sup>a</sup> Qianpeng Zhang,<sup>b</sup> Hexiang He,<sup>c</sup> Shuang Xiao,<sup>d</sup> Zhiyong Fan,<sup>b</sup> Kam Sing Wong<sup>c</sup> and Shihe Yang<sup>a,d,\*</sup>

In this work, we have designed a mesoporous TiO<sub>2</sub> nanobowl (NB) array with pore size, bowl size and film thickness being easily controllable by the sol-gel process and the polystyrene (PS) template diameter. Based on the TiO<sub>2</sub> NB array, we fabricated carbon cathode based perovskite solar cells (C-PSCs) to investigate the impact of TiO<sub>2</sub> NB nanostructures on the performance of the as-obtained C-PSCs devices. As expected, the TiO<sub>2</sub> NB based devices show higher power conversion efficiency (PCE) than that of the planar counterpart, mainly due to the enhanced light absorption arising from the NB-assisted light management, the improved pore-filling of high quality perovskite crystals and the increased interface contacts for rapid electron extraction and fast charge transport. Leveraging these advantages of the novel TiO<sub>2</sub> NB film, the 220 nm-PS templated TiO<sub>2</sub> NB based devices performed the best on both light absorption capability and charge extraction, and achieved a PCE up to 12.02% with good stability, which is 37% higher than that of the planar counterpart. These results point to a viable and convenient route toward fabrication of TiO<sub>2</sub> ETL nanostructures for high performance PSCs.

### 1. Introduction

Organic-inorganic lead halide perovskite-based mesoscopic or planar heterojunction (PHJ) solar cells have experienced an overwhelming surge in power conversion efficiency (PCE) in the past few years due to their superior photovoltaic properties such as broad light absorption spectra range, high extinction coefficient, long charge-carrier diffusion length, and ambipolar transport.<sup>1-12</sup> Recently, with a suitable work function and electrical conductivity, cheap and abundant carbon materials were successfully used for the cathodes for hole transport material (HTM)-free perovskite solar cell (C-PSCs), and opened up a new era for low-cost, high efficiency PSCs.<sup>13-15</sup> Aside from the low-cost as a result of the elimination of HTM and noble metal and the simplification of device fabrication, the C-PSCs also have the potential to overcome the moisture sensitive bottleneck of the halide perovskites thanks to the hydrophobic properties and the good stability of carbon materials.<sup>16-21</sup> However, the replacement of HTM and metal

electrode with the carbon materials hinges on the resolution of some of the current problems involving the nanomaterials and interface engineering. First among the problems is the relatively slow hole extraction, which leads to increased charge recombination and thus the low open-circuit voltage ( $V_{oc}$ ).<sup>13</sup> Second, the low light harvesting efficiency (low IPCE) in the long wavelength range from 500 to 800 nm (for methylammonium lead iodide, MAPbI<sub>3</sub>) turns up as a key issue because of the absence of light back-scattering from metal electrodes and the insufficient charge separation at low photon energies.<sup>22-25</sup> Therefore, it is urgent to engineer nanomaterials and interfaces to optimize the performance of C-PSCs while retaining their distinct advantages of low cost, good stability and simple fabrication process.

In the meantime, the improvements of C-PSCs have been mainly propelled by working up the device architectures,<sup>26-28</sup> carbon electrode materials and interfaces,<sup>29-33</sup> perovskite crystal quality and compositions,<sup>34-36</sup> and electron transporting layer (ETL) structures and interfaces.<sup>37-39</sup> It is widely recognized that optical and electronic properties of the ETLs as well as the ETL/perovskite interface are of importance to the efficiency of PSCs.<sup>40,41</sup> Until now, mesoporous TiO<sub>2</sub> nanoparticle films are the most commonly used ETLs, which serve as a scaffold to support the perovskite layer and facilitate the interfacial charge transfer and the following charge transport, and thereby have enabled by far the best device performance with reduced hysteresis.<sup>9,42,43</sup> Intriguingly, the PSC efficiency is strongly related to the thickness of the TiO<sub>2</sub> scaffold layer: a thick TiO<sub>2</sub> film can scaffold a thick perovskite absorber layer with strong light absorption.<sup>42,44,45</sup> However, the thick TiO<sub>2</sub> film also means numerous interfaces and strong carrier recombination, which would encumber the perovskite pore-filling and slow down

<sup>a</sup> Department of Chemistry, The Hong Kong University of Science and Technology, Clear Water Bay, Kowloon, Hong Kong.

<sup>b</sup> Department of Electronic and Computer Engineering, The Hong Kong University of Science and Technology, Clear Water Bay, Kowloon, Hong Kong.

<sup>c</sup> Department of Physics, The Hong Kong University of Science and Technology, Clear Water Bay, Kowloon, Hong Kong.

<sup>d</sup> Nano Science and Technology Program, The Hong Kong University of Science and Technology, Clear Water Bay, Kowloon, Hong Kong.

<sup>†</sup> These authors contributed equally to this work.

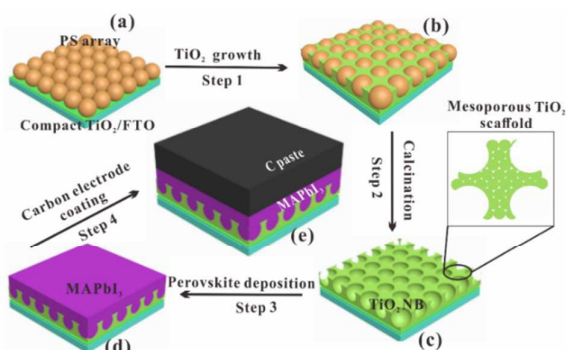
\* Corresponding author, Email: chsyang@ust.hk

Electronic Supplementary Information (ESI) available: Experimental details; Text, Tables and Figures giving detailed and additional material characterizations. See DOI: 10.1039/x0xx00000x

charge collection.<sup>46</sup> Conversely, a thin TiO<sub>2</sub> film results in good charge transport but poor light harvesting.<sup>47</sup> Moreover, PSCs based on ultrathin TiO<sub>2</sub> films in terms of the PHJ structure have shown large hysteresis, highlighting the need of predictive control over the perovskite film morphology.<sup>22</sup>

In order to balance the fast charge transport and efficient light harvesting, herein we have designed a TiO<sub>2</sub> nanobowl (TiO<sub>2</sub> NB) array film as an alternative ETL for C-PSCs. The TiO<sub>2</sub> nanobowl (TiO<sub>2</sub> NB) array film was fabricated by combining the colloidal template and liquid phase deposition methods. The resulting TiO<sub>2</sub> NB array film is ordered and offers flexible dimensional and thickness control by changing the polystyrene (PS) diameter in the monolayer packing of PS spheres and the sol-gel processing conditions. Enhanced PCE was obtained due to predominant role of the TiO<sub>2</sub> NB structure in promoting light harvesting,<sup>48-53</sup> increasing surface area, and improving perovskite crystalline quality. Moreover, the macroporous structure with hollow NB allowed perovskite to easily penetrate into the ETL and thus form an intimate perovskite/TiO<sub>2</sub> interface, which, together with the specially prepared thin compact TiO<sub>2</sub> film, facilitates the charge separation and transport. We have systematically studied the TiO<sub>2</sub> film parameters on the photovoltaic performance, and achieved up to 12.02% PCEs, underpinning the TiO<sub>2</sub> NB array film as a promising perovskite host for understanding the structure-performance relationship of C-PSCs in depth and for bringing C-PSCs into commercially viable devices.

## 2. Results and discussion



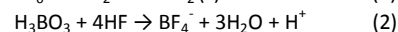
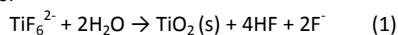
**Figure 1.** Schematic fabrication procedure for the TiO<sub>2</sub> NB array film based C-PSCs. (a) PS monolayer; (b) PS monolayer filled with TiO<sub>2</sub> sol; (c) TiO<sub>2</sub> NB array film; (d) perovskite filled and topped TiO<sub>2</sub> NB array; (e) the wrought C-PSC.

Figure 1 schematizes the process for the synthesis of C-PSCs based on monolayer TiO<sub>2</sub> NB ETL, which was prepared by the PS-template method. As shown, the monolayer TiO<sub>2</sub> NB film was templated straightforwardly by ordered PS arrays, which were fabricated as mono- or bi-layer films on a compact TiO<sub>2</sub> coated FTO substrate via the solvent-evaporation-induced self-assembly method (Figure S1 and S2, Supporting Information). Subsequently, the macroporous PS arrays were filled with mesoporous TiO<sub>2</sub> by a liquid phase deposition method at room temperature (step 1), forming a monolayer TiO<sub>2</sub> NB film with dual porosity after slow

calcination (step 2). Herein, different pore sizes and thicknesses of TiO<sub>2</sub> NB films were fabricated by introducing various diameters of PS spheres (180 nm, 220 nm, 500 nm, Figure S2). Onto the porous TiO<sub>2</sub> NB films, CH<sub>3</sub>NH<sub>3</sub>PbI<sub>3</sub> (MAPbI<sub>3</sub>) perovskite was then deposited by a modified two-step solution method (step 3). Finally, carbon (C) paste was directly coated on the perovskite film via doctor-blading, thus averting the extra deposition of expensive HTM and noble metal electrode (step 4). For convenience, hereafter, we designate various TiO<sub>2</sub> NB structures as “TiO<sub>2</sub> NB-x-P”, where x refers to the diameters (nm) of PS template and P represents deposition of perovskite MAPbI<sub>3</sub>. More experimental details about the TiO<sub>2</sub> NB film formation and device fabrication procedure are given in Supporting Information (Experimental Methods).

### 2.1. Formation of TiO<sub>2</sub> NB array

Liquid phase deposition method was used to prepare the TiO<sub>2</sub> NB films through reactions of ammonium hexafluorotitanate ((NH<sub>4</sub>)<sub>2</sub>TiF<sub>6</sub>, 0.05 M) and boric acid (H<sub>3</sub>BO<sub>3</sub>, 0.15 M) within PS array templates.<sup>54,55</sup> More specifically, the deposition reactions can be expressed as:



Here the H<sub>3</sub>BO<sub>3</sub> serves as an F<sup>-</sup> scavenger (equation (2)) and thus accelerates the hydrolysis reaction (equation (1)). In this way, the TiO<sub>2</sub> film thickness can be easily controlled by the reaction time and PS diameters.

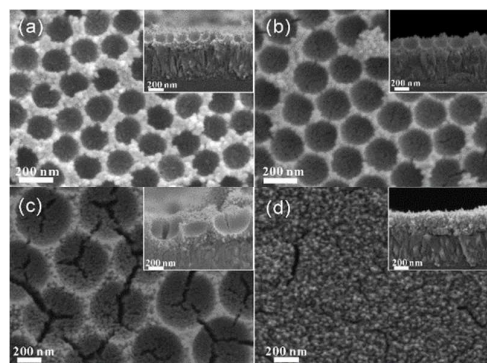


**Figure 2.** Top-view and the corresponding cross-sectional SEM images (insets) of (a) TiO<sub>2</sub> NB-180, (b) TiO<sub>2</sub> NB-220, (c) TiO<sub>2</sub> NB-500, and (d) planar TiO<sub>2</sub>.

Figure 2 shows scanning electron microscopy (SEM) images of as-obtained monolayer ordered TiO<sub>2</sub> NB arrays along with a planar TiO<sub>2</sub> film for comparison. Clearly, the TiO<sub>2</sub> films prepared by the liquid phase deposition method are all composed of mesoporous TiO<sub>2</sub> nanoparticles with a size of 20–25 nm (Figure 2 and enlarged SEM image shown in Figure S3). The diameters of the individual TiO<sub>2</sub> NBs are found to be 160 nm, 200 nm, and 470 nm with a 25–50 nm connective vein for TiO<sub>2</sub> NB-180, TiO<sub>2</sub> NB-220, and TiO<sub>2</sub> NB-500, respectively. The decreased diameters of the TiO<sub>2</sub> NB compared to the PS templates can be ascribed to the volume shrinking during the calcination process. Cross-sectional SEM characterizations (insets) testifies the uniform distribution of monolayer TiO<sub>2</sub> NBs and the good connection with the compact TiO<sub>2</sub> coated on FTO. The heights

of the monolayer TiO<sub>2</sub> NBs are 150 nm, 180 nm, and 300 nm, each on a 75 nm compact layer, for TiO<sub>2</sub> NB-180, TiO<sub>2</sub> NB-220, and TiO<sub>2</sub> NB-500, respectively, which are uniformly smaller than the corresponding NB diameters, especially for larger NBs, due to gravity enhanced vertical shrinking. For comparison, a planar TiO<sub>2</sub> film 240 nm thick was also prepared on an identical TiO<sub>2</sub> compact layer by the same procedure but without the PS template (Figure 2d). It should be pointed out that cracks are clearly observed in the films, especially in the TiO<sub>2</sub> NB-500 and planar TiO<sub>2</sub> films, that is, when the films become thick. The cracks are caused by stress generated during the growth and calcination processes, which increases with the film thickness. Actually, to our advantage, the presence of NBs decreases the effective TiO<sub>2</sub> film thickness, which would lessen the cracking, and the open hemisphere-like structure increases the effective perovskite/TiO<sub>2</sub> interface area, which would ease the full-filling of perovskite crystals and thus facilitates the charge separation/transport.

## 2.2. Perovskite and carbon electrode deposition

The synthesized TiO<sub>2</sub> NB films were then used for the deposition of MAPbI<sub>3</sub>. As shown in Figure 3a-d, MAPbI<sub>3</sub> perovskite densely covers the entire TiO<sub>2</sub> film with a capping layer of about 400-500 nm. Top-view SEM images (Figure S4a-d) also show that dense and uniform perovskite crystals with a size of 100-250 nm have been deposited on the TiO<sub>2</sub> NB architectures, whereas obvious pinholes (shown by white dotted circles in Figure S4d) can be found in the planar TiO<sub>2</sub> sample. To better understand how the TiO<sub>2</sub> NB films influence the perovskite crystals grown above, we also monitored morphologies of the PbI<sub>2</sub> films deposited on the TiO<sub>2</sub> NB-220 and planar TiO<sub>2</sub> films by SEM (Figure S5). Noticeably, a large and dense PbI<sub>2</sub> crystal layer with a thickness of ~ 310 nm (capping layer) was formed on the TiO<sub>2</sub> NB-220 film, whereas a thinner PbI<sub>2</sub> capping layer (~ 260 nm) with obvious pinholes was formed on the planar TiO<sub>2</sub> film. It has been well established that a high quality PbI<sub>2</sub> film is a prerequisite for growing a dense and highly crystalline perovskite layer.<sup>56</sup> Thus the dense PbI<sub>2</sub> and perovskite films with a full coverage on the TiO<sub>2</sub> NB film indicate that the surface patterned TiO<sub>2</sub> NB film could serve as a good scaffold for growing the uniform PbI<sub>2</sub> capping layer and thus for facilitating the formation of the dense perovskite crystalline layer.<sup>57</sup> Moreover, the open macropores of TiO<sub>2</sub> NB can promote intimate TiO<sub>2</sub>/perovskite interface formation, whereas the small interface in the planar TiO<sub>2</sub> film appears to be insufficient to guide the crystal growth of perovskite, thus resulting in the pinhole formation. Understandably, controlling the crystal growth of perovskite has a significant impact on the charge carrier mobility and interfacial charge separation rate.<sup>58,59</sup> Thanks to the uniform perovskite crystals, they can form intimate interface with carbon cathode without obvious gaps (Figure 3e).

Compositions of the perovskite films on TiO<sub>2</sub> NB and planar substrates were investigated by X-ray diffraction (XRD). As shown in Figure 3f, the strong Bragg peaks at 14.03°, 28.37°, 31.79°, and 43.10° can be assigned respectively to (110), (220), (310), and (330) of MAPbI<sub>3</sub>, which are subsumed in the tetragonal phase.<sup>25</sup> Unlike the conventional two-step method reported previously, the MAI (1 mg/ml) in cyclohexane (CHex)/isopropanol (IPA) = 9/1 (v/v) mixed

solvent was used to convert pre-formed lead iodide (PbI<sub>2</sub>) film into perovskite. In the mixed solution, the "Ostwald ripening" effect of MAPbI<sub>3</sub> crystal can be effectively suppressed by the cyclohexane which acts as antisolvent to allow controlled crystallization at a low concentration of MAI. SEM images and XRD patterns of the MAPbI<sub>3</sub> perovskite film prepared by a conventional sequential solution method using pure IPA are also shown in Figure S6 for comparison. Obviously, the crystal sizes of the pure IPA deposited MAPbI<sub>3</sub> vary greatly from 70-100 nm of small crystals to 500-600 nm of large crystals; the large crystals protrude out from the film, which are much larger than those prepared from the CHex/IPA mixed solvent (100-250 nm). The large crystals protruding out of the film would result in the formation of apparent gaps at the interface of the carbon electrode and perovskite (Figure S6f). Meanwhile, on comparing the XRD patterns, we notice a characteristic peak of PbI<sub>2</sub> at 12.50° for the pure IPA deposited perovskite film (Figure S6g), indicating the incompletely converted PbI<sub>2</sub> even with a high concentration of MAI.<sup>60</sup> In contrast, the absence of the peak of PbI<sub>2</sub> at 12.50° for the CHex/IPA mixed solvent deposited perovskite film connotes the complete conversion of PbI<sub>2</sub>, which is auspicious for high photoelectronic performance.

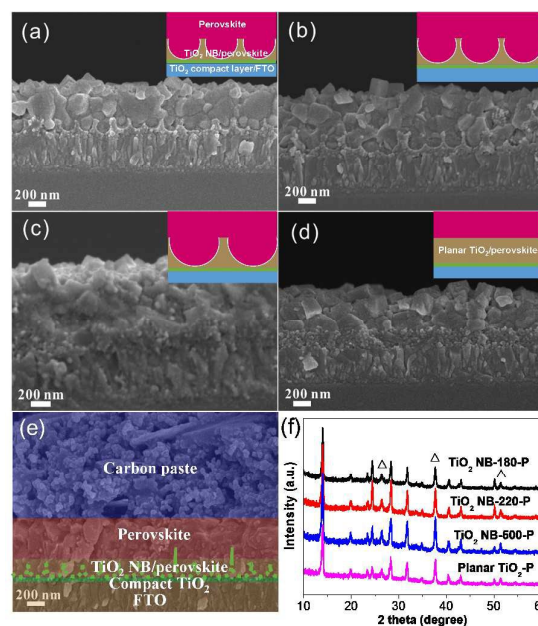


**Figure 3.** Cross-sectional SEM images of (a) TiO<sub>2</sub> NB-180-P, (b) TiO<sub>2</sub> NB-220-P, (c) TiO<sub>2</sub> NB-500-P, and (d) planar TiO<sub>2</sub>-P. The corresponding schematic diagrams in the insets of (a-d) show the structures of perovskite-deposited TiO<sub>2</sub> films. (e) Cross-sectional SEM image of C-PSC device based on TiO<sub>2</sub> NB-220-P. (f) XRD patterns of perovskite deposited on different TiO<sub>2</sub> films.  $\Delta$  represents the XRD peaks of FTO.

## 2.3. Photovoltaic performance

Figure 4 shows photovoltaic performance characteristics of four representative C-PSCs based on the TiO<sub>2</sub> NBs and planar TiO<sub>2</sub> films. The photocurrent-voltage (*J-V*) curves of the C-PSCs shown in Figure 4a were measured under standard global AM 1.5, 100 mW/cm<sup>2</sup>

light illumination, and the measured parameters are summarized in Table 1. Obviously, devices based on TiO<sub>2</sub> NB show higher efficiency than that based on the planar TiO<sub>2</sub> film, and in more detail, one notices a dependence of the TiO<sub>2</sub> NB size on photovoltaic performance. The highest PCE of 12.02% was achieved for the TiO<sub>2</sub> NB-220-P based C-PSC, with an open-circuit voltage ( $V_{oc}$ ) of 1.00 V, a short-circuit current density ( $J_{sc}$ ) of 22.67 mA/cm<sup>2</sup> and a fill factor ( $FF$ ) of 0.53. Notably, the PCE improvement for TiO<sub>2</sub> NB based C-PSCs, with increased  $J_{sc}$ ,  $V_{oc}$ , and  $FF$ , especially  $J_{sc}$ , stems for the most part from the improved perovskite/TiO<sub>2</sub> interface and the increased light harvesting efficiency due to the unique architecture of the TiO<sub>2</sub> NB arrays. The different performance of the TiO<sub>2</sub> NB based C-PSCs might result from the varied pore sizes and film thicknesses, which might influence the perovskite crystal deposition and thus the charge transport and light management property. As evidently demonstrated by the dark  $J$ - $V$  curves in Figure 4a, devices fabricated from TiO<sub>2</sub> NB show much higher dark current onset than that of the planar TiO<sub>2</sub> film based device. This is indicative of effectively inhibited charge recombination in the TiO<sub>2</sub> NB based devices.<sup>25</sup> To further check the reproducibility of the PSCs, the histograms of the  $V_{oc}$ ,  $J_{sc}$ ,  $FF$  and PCE for a batch of 20 devices based on TiO<sub>2</sub> NB-180-P, TiO<sub>2</sub> NB-220-P, TiO<sub>2</sub> NB-500-P and planar TiO<sub>2</sub>-P are shown in Figure S7 and the statistics are summarized in Table S1. The small standard deviations indicate good device reproducibility. For comparison, TiO<sub>2</sub> NB-220-P based C-PSCs with the conventional pure IPA solution deposited perovskite film were also prepared, and the optimized device gave a  $V_{oc}$  of 0.98 V, a  $J_{sc}$  of 21.59 mA/cm<sup>2</sup>, a  $FF$  of 0.51, and a PCE of 10.79% (Figure S8), showing an inferior photovoltaic performance than that prepared with the mixed CHex/IPA solvent (12.02%). The incomplete PbI<sub>2</sub> conversion and inferior perovskite/carbon interface could therefore be the explanation for the significantly decreased PV performance.

(0.74 V) under on-off illumination cycles for TiO<sub>2</sub> NB-220-P based C-PSC.

**Table 1.** PV Performances of C-PSCs based on TiO<sub>2</sub> NB architectures with varied pore sizes and planar TiO<sub>2</sub> for comparison.

Samples	$V_{oc}$ (V)	$J_{sc}$ (mA/cm <sup>2</sup> )	$FF$	PCE (%)	Integrated $J_{sc}^a$ (mA/cm <sup>2</sup> )
TiO <sub>2</sub> NB-180-P	0.98	21.80	0.53	11.32	19.82
TiO <sub>2</sub> NB-220-P	1.00	22.67	0.53	12.02	20.71
TiO <sub>2</sub> NB-500-P	0.98	20.18	0.51	10.09	18.41
Planar TiO <sub>2</sub> -P	0.97	18.07	0.50	8.76	17.38

<sup>a</sup> Integrated  $J_{sc}$  from the IPCE curves shown in Figure 4b.

Figure 4b shows incident-photon-to-current conversion efficiency (IPCE) spectra for the four representative C-PSCs based on TiO<sub>2</sub> NB and planar TiO<sub>2</sub>. Like most of the reported C-PSCs, the planar TiO<sub>2</sub>-P based cell exhibits IPCE values of above 80% at <550 nm and decreases dramatically in the long wavelength range. The use of TiO<sub>2</sub> NB arrays brings in a noticeable IPCE improvement in the long wavelength range of 500-760 nm, mainly due to the increased effective light harvesting and/or charge extraction, which will be discussed below.<sup>61</sup> This IPCE enhancement correlates well with the higher photocurrent in the TiO<sub>2</sub> NB based C-PSCs. Integrating the overlap of the IPCE spectrum yield a photocurrent density of 19.82, 20.71, 18.41, and 17.38 mA/cm<sup>2</sup> for TiO<sub>2</sub> NB-180-P, TiO<sub>2</sub> NB-220-P, TiO<sub>2</sub> NB-500-P and planar TiO<sub>2</sub>-P, which are in excellent agreement with the measured photocurrent density (Figure 4a and Table 1). It has been widely recommend that monitoring the stabilized current density at the maximum output power point is a useful parameter to present the cell performance alongside the  $J$ - $V$  scan derived PCE.<sup>25,62</sup> We thus recorded the photocurrent density of the four representative C-PSCs based on TiO<sub>2</sub> NB and planar TiO<sub>2</sub> at a function of time held at the maximum output power point (Figure 4c). As shown in Figure 4c, the photocurrent density of the devices based on TiO<sub>2</sub> NB arrays stabilize quickly within seconds and yield a stabilized PCE around 11.13%, 11.80%, and 9.82% for TiO<sub>2</sub> NB-180-P, TiO<sub>2</sub> NB-220-P, and TiO<sub>2</sub> NB-500-P, respectively, measured 300 s after. However, a continuously increase of the photocurrent density is observed for the planar TiO<sub>2</sub>-P based C-PSC yielding a stabilized PCE of around 8.57%; the lower performance could originate from the inferior perovskite/TiO<sub>2</sub> interface, such as the one with pinholes mentioned above.

In addition, the photocurrent density-time profile at the maximum output power point under on-off illumination cycles for TiO<sub>2</sub> NB-220-P based C-PSC was recorded (Figure 4d) and a fast photo-response to light on and off is evident, indicating the fast electron transfer due to the intimate interface of TiO<sub>2</sub> NB-220-P/perovskite. The stability of the champion TiO<sub>2</sub> NB-220-P based C-PSC at ambient condition was also investigated (Figure S9). Significantly, only a slight PCE decrease was observed for the champion C-PSC; the PCE decline was from 12.02% to 11.09% with an 8% drop after 45 days' storage without any encapsulation (humidity 10-20%), indicating a good stability of the C-PSCs mainly due to the high quality of perovskite crystalline films, intimate interface between perovskite and TiO<sub>2</sub> NB and the compact carbon

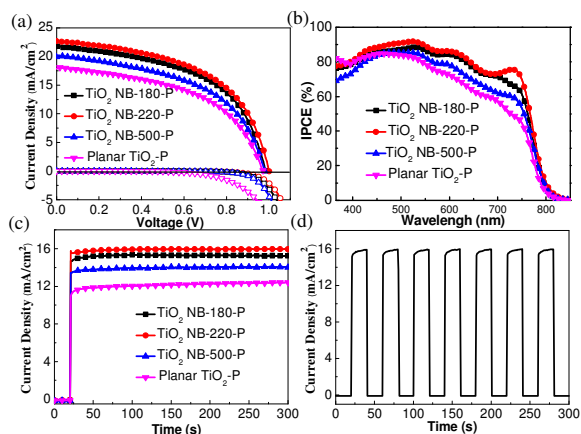


**Figure 4.** Comparison of the photovoltaic performance of the C-PSCs devices based on different TiO<sub>2</sub> films. (a) Characteristic  $J$ - $V$  and dark  $J$ - $V$  plots, and (b) the IPCE spectra of the C-PSCs devices based on different TiO<sub>2</sub> films. (c) Photocurrent density as function of time for the devices held at the maximum output power point (0.73 V, 0.74 V, 0.70 V and 0.69 V for TiO<sub>2</sub> NB-180-P, TiO<sub>2</sub> NB-220-P, TiO<sub>2</sub> NB-500-P, and Planar TiO<sub>2</sub>-P, respectively). (d) Photocurrent density as a function of time held at the maximum output power point

electrode.<sup>17</sup> Moreover, to detect any hysteresis in the devices, the  $J$ - $V$  curves of the C-PSCs based on different  $\text{TiO}_2$  films were further measured via the forward and backward scans with a scan rate of 10 mV/s. Obviously, the  $\text{TiO}_2$  NB films based C-PSCs, especially the  $\text{TiO}_2$  NB-220-P based C-PSC, show smaller hysteresis than the planar  $\text{TiO}_2$  film based C-PSCs (Figure S10). The origin of the  $I$ - $V$  hysteresis has been widely studied, and the degree of hysteresis strongly depends on the quality of the perovskite and the mesoporous  $\text{TiO}_2$  layers as well as their interface.<sup>62</sup> Considering that these four C-PSCs have a similar cell configuration and used the same perovskite deposition method, it is believed that the different performance with respect to the hysteresis effect is due to the different interface quality of  $\text{TiO}_2$ /perovskite which directly influences the electron transfer and transport processes. By combing the SEM results in Figure 3 and the hysteresis investigation in Figure S10, we submit that the  $\text{TiO}_2$  NB array architecture provides a more favorable interface for electron collection.

#### 2.4. Structure-performance correlation – light trapping

For PSCs, multiple factors determine the photovoltaic performance. To understand the origin of the PCE improvement for the  $\text{TiO}_2$  NB based C-PSCs, we first examine the optical properties of the devices. For comparison of the light management properties of the  $\text{TiO}_2$  NB array film with different pore sizes and the planar film, UV-vis optical properties were measured using an integrating sphere for the propagation of incident light from the glass side. First, the transmittance of ETL-coated FTO substrate could significantly affect the capture of incident light by the perovskite active layer, and was thus carefully measured using FTO as a control sample. Figure 5a shows the transmittance spectra of  $\text{TiO}_2$  NB arrays with varied NB sizes and the planar  $\text{TiO}_2$  film on FTO. Interestingly, the transmittance is strongly dependent on the geometry and thickness of the  $\text{TiO}_2$  films. Particularly noteworthy is that FTO substrates coated with  $\text{TiO}_2$  NB-180 and  $\text{TiO}_2$  NB-220 films show better transmittance than the bare FTO over the wavelength ranges of 530-650/730-800 nm and 500-650/750-800 nm, respectively, mainly due to the effective anti-reflective effect of the  $\text{TiO}_2$  NB array film.<sup>63,64</sup> The slightly transmittance difference between  $\text{TiO}_2$  NB-180 and  $\text{TiO}_2$  NB-220 film is because the anti-reflective effect is thickness-dependent.<sup>65,66</sup> Also, it is observed that the transmittance of  $\text{TiO}_2$  NB-500 is higher than that of planar  $\text{TiO}_2$  especially in the range of 500-800 nm, indicating that the unique geometry of  $\text{TiO}_2$  NB array can facilitate the light transmittance. However, for the sample of  $\text{TiO}_2$  NB-500, the transmittance is decreased between 440-800 nm compared with those of  $\text{TiO}_2$  NB-180 and  $\text{TiO}_2$  NB-220, probably due to the increased Rayleigh scattering from the  $\text{TiO}_2$  nanoparticles for the increased film thickness (insets in Figure 2).<sup>67</sup>

We next examine the diffuse reflectance spectra of the  $\text{TiO}_2$  films shown in Figure 5b. In general, the  $\text{TiO}_2$  NB films exhibit a significant suppression of reflection over a broad spectral range compared with the planar film. The average reflectance of the  $\text{TiO}_2$  NB-coated FTO is significantly suppressed to be below 15% throughout the whole wavelength range, especially for the  $\text{TiO}_2$  NB-180 and  $\text{TiO}_2$  NB-220 films, in keeping with the transmittance results. Such increased transmittance and broadband anti-reflection of the  $\text{TiO}_2$

NB array-coated FTO can be ascribed to the light management ability of the unique 3D geometry and the 2D periodic structure. Simply from the classical electrodynamics, the  $\text{TiO}_2$  NB array with sub-wavelength features imparts a smooth refractive index transition (the so-called graded refractive index) like the moth-eye, and thereby effectively suppresses light reflection and increases the light transmittance.<sup>65</sup>

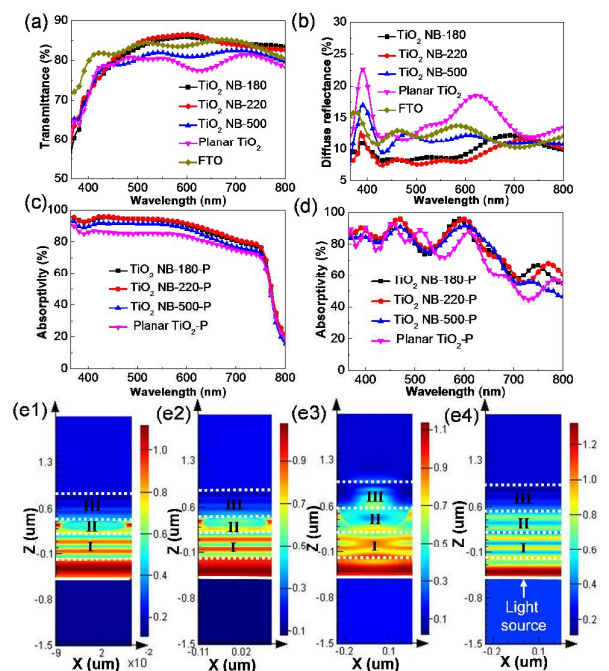


**Figure 5.** (a) Optical transmittance spectra and (b) reflectance spectra of different  $\text{TiO}_2$  films and FTO, (c) experimental and (d) simulated absorptivity spectra of perovskite films deposited on different  $\text{TiO}_2$  films. (e) Simulated cross-sectional  $|E|^2$  distribution of the EM wave at 600 nm wavelength in the perovskite deposited (e1)  $\text{TiO}_2$  NB-180-P, (e2)  $\text{TiO}_2$  NB-220-P, (e3)  $\text{TiO}_2$  NB-500-P, and (e4) planar  $\text{TiO}_2$ -P, the ranges between the white dotted lines represent (I) FTO, (II)  $\text{TiO}_2$  compact layer +  $\text{TiO}_2$  ETL/perovskite, and (III) perovskite capping layer.

To further investigate the light management property of the  $\text{TiO}_2$  NB arrays, absorptivity spectra (A) of the perovskite films on different  $\text{TiO}_2$  films were extracted from the measured reflectance (R) and transmittance (T) spectra through the relation of  $A = 1 - R - T$  (Figure S11). As shown in Figure 5c, the absorptivity of the  $\text{TiO}_2$  NB based perovskite films is remarkably enhanced compared with the planar  $\text{TiO}_2$ -P, and among them, the  $\text{TiO}_2$  NB-180-P and  $\text{TiO}_2$  NB-220-P films show higher broadband absorptivity than the  $\text{TiO}_2$  NB-500-P film. Notably, compared to the  $\text{TiO}_2$  NB-180-P,  $\text{TiO}_2$  NB-220-P presents even higher absorption, mainly due to its superior anti-reflection property (Figure 5a,b and Figure S8a,b), which is held responsible for the  $J_{sc}$  enhancement shown in Figure 4a.

In order to further verify the experimental results, finite-difference-time-domain (FDTD) simulations were performed on these films. Gratifyingly, the simulated absorptivity spectra (Figure

5d) show a quite consistent trend over all the wavelengths with the experimental counterparts (Figure 5c). The higher absorptivity above 700 nm in the simulated absorptivity spectra is mainly due to the perfect perovskite film in the simulated model compared with the practical ones, which would lead to lower transmittance and thus higher absorptivity in the long wavelength range (Figure S11). In addition, the big oscillation in the simulated absorptivity spectra results from the simulation employing perfect surfaces and interfaces, which lead to constructive and/or destructive interference, in contrast to real experiments wherein the surface and interfaces will be rough.

To shed light on how light is coupled into the films, the cross-sectional electric field intensity ( $|E|$ ) distributions of the electromagnetic (EM) wave at 600 nm are calculated and shown in Figure 5e. In these simulation models, EM plane waves propagate upward from  $Z = -0.5 \mu\text{m}$  and reach the FTO bottom surfaces at  $Z = 0.2 \mu\text{m}$ . Note that the color index at the specific location in the cross-sectional  $|E|$  distribution indicates the magnitude of  $|E|$  at that point.<sup>68,69</sup> The refractive index (RI) of perovskite was used according to the literature,<sup>70</sup> and the RI of FTO,  $\text{TiO}_2$  compact layer and mesoporous  $\text{TiO}_2$  layer were measured by ellipsometry (the RI data of different layers are shown in Figure S12). In order to facilitate the observation of light propagation, white dotted lines are used in Figure 5e1-e4 to show the edges of individual material layers in the devices. The fringe patterns in Figure 5e above  $Z = -0.5 \mu\text{m}$  originate from interference between the light source and the reflected light, and the color index below  $Z = -0.5 \mu\text{m}$  indicates the intensity of reflected light.<sup>69</sup> The cross-sectional  $|E|$  distributions reveal a lower reflection for the  $\text{TiO}_2$  NB-180-P (Figure 5e1) and  $\text{TiO}_2$  NB-220-P (Figure 5e2) films than the  $\text{TiO}_2$  NB-500-P (Figure 5e3) and planar  $\text{TiO}_2$ -P (Figure 5e4) films, as indicated by the darker color below the light source due to their antireflective effect associated with the smaller-sized NB arrays. Interestingly, the color patterns in the II and III regions in Figure 5e illustrate that the  $\text{TiO}_2$  NB array based samples have much stronger electric field intensity inside the mesoporous  $\text{TiO}_2$  ETL layer and the perovskite capping layer than the planar based sample. This is because more incident photons are coupled into the  $\text{TiO}_2$  NB array based samples due to their superior antireflection effect, which is beneficial for light absorption by the perovskite absorber to generate charge carriers. However, for the  $\text{TiO}_2$  NB-500-P sample, the stronger reflection than that is the  $\text{TiO}_2$  NB-180-P and  $\text{TiO}_2$  NB-220-P samples results in a lower light absorption, in accord with the lower  $J_{sc}$  as presented in Figure 4a.

In the above, the combination of optical measurements and simulation investigation has shown the potency of the  $\text{TiO}_2$  NB arrays with an appropriate pore size and thickness for photon capturing. Previous studies have demonstrated that  $\text{TiO}_2$  NB arrays possess a graded refractive index feature like moth-eye, so incident light rays tend to be bent progressively, effectively suppressing light reflection (Figure S13-I)<sup>65,66</sup> and thereby increasing light absorption. From another perspective, as light passes through the periodic  $\text{TiO}_2$  NB array, multiple internal reflections increase the effective light path in the active layer, which are more obvious in  $\text{TiO}_2$  NB arrays with an NB size comparable to the light wavelength (Figure S13-II).<sup>67,71,72</sup> On the other hand, proper pore size (pitch) and thickness of  $\text{TiO}_2$  NB films should be designed to minimize light loss through strong backward scattering (predominated by Rayleigh and Mie

scattering from nanoparticles and pores).<sup>73-76</sup> The stronger backward scattering could explain the inferior transmittance and anti-reflectance of  $\text{TiO}_2$  NB-500-P than that of  $\text{TiO}_2$  NB-180-P and  $\text{TiO}_2$  NB-220-P due to its larger pore size and film thickness. The slightly better anti-reflectance effect of  $\text{TiO}_2$  NB-220-P than that of  $\text{TiO}_2$  NB-180-P may also be ascribed to the appropriate film thickness that can optimize light bending without very strong back scattering effect.<sup>65</sup> Therefore, a periodic  $\text{TiO}_2$  NB array structure with an appropriate pore size and film thickness in the front of a device can reduce reflection losses and thus effectively enhance the light absorption in the active layer, leading to improved  $J_{sc}$ .

## 2.5. Structure-performance correlation – charge transfer

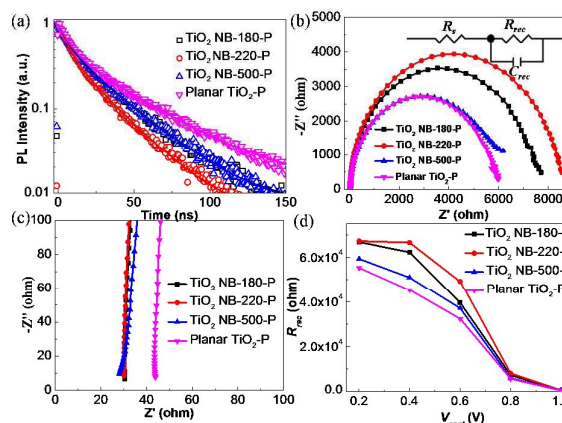


**Figure 6.** (a) Time-resolved PL measurements taken at the peak emission wavelength of perovskite deposited upon different  $\text{TiO}_2$  films after excitation at 400 nm (3.8 MHz, 55  $\mu\text{W}$ ). The solid lines in (a) are the biexponential fits of the PL decay transients. (b, c) Nyquist plots of C-PSCs based on different  $\text{TiO}_2$  films in the dark at a bias voltage of 0.8 V, equivalent circuit is in the inset of (b). (d) Recombination resistance ( $R_{rec}$ ) as a function of applied bias voltage ( $V_{app}$ ) curves for C-PSCs based on different  $\text{TiO}_2$  films.

For the different  $\text{TiO}_2$  architectures based C-PSCs, the capability of extracting electrons through the perovskite/ $\text{TiO}_2$  interface is also of great importance for the photovoltaic performance. Thus, the electron transfer kinetics were evaluated by means of time-resolved photoluminescence (TRPL) characterizations.<sup>8,77</sup> Figure 6a shows the room temperature TRPL profiles of perovskite deposited on  $\text{TiO}_2$  NB arrays and planar  $\text{TiO}_2$ . Note that there is no carbon electrode in these films so that we can focus on the perovskite/ $\text{TiO}_2$  interface. The PL decays were fitted by global biexponential model and the detailed fitted PL lifetimes ( $\tau_1$ ,  $\tau_2$ , and  $\tau$ ) are collected in Table 2.<sup>78,79</sup> For simplicity, the weighted average value of  $\tau_1$  and  $\tau_2$  is utilized to represent the PL lifetime ( $\tau$ , Table 2). As illustrated in Figure 6a, an enhanced PL quenching rate is observed with the  $\text{TiO}_2$  NBs, and the fitted PL lifetime follows the sequence as  $\tau$  ( $\text{TiO}_2$  NB-220-P) <  $\tau$  ( $\text{TiO}_2$  NB-180-P) <  $\tau$  ( $\text{TiO}_2$  NB-500-P) <  $\tau$  (planar  $\text{TiO}_2$ -P). The PL quenching rate is expected to originate from the charge-carrier extraction across the interface, and it suggests that the photoinduced electrons in perovskite could be more efficiently extracted by the  $\text{TiO}_2$  NB arrays due to their increased interfacial

area and contact with perovskite.<sup>77</sup> Presumably, for TiO<sub>2</sub> NB-220-P, the appropriate TiO<sub>2</sub> film thickness and pore size could have contributed to the efficient electron extraction by promoting the quality of the perovskite deposition and the interface contact. In short, the high PCE of the TiO<sub>2</sub> NBs based C-PSCs results not only from the enhanced light-management property but also from the enhanced charge extraction stemming from the unique 3D NB array architecture.

**Table 2.** Fitted PL lifetimes ( $\tau_1$ ,  $\tau_2$ , and  $\tau$ ) of perovskite deposited upon different TiO<sub>2</sub> films, and the fitting parameters series resistance ( $R_s$ ) and recombination resistance ( $R_{rec}$ ) obtained from EIS data using the equivalent circuit in Figure 6b.

Samples	$\tau_1$ (ns) <sup>a</sup>	$\tau_2$ (ns) <sup>a</sup>	$\tau$ (ns) <sup>a</sup>	$R_s$ (ohm)	$R_{rec}$ (ohm)
TiO <sub>2</sub> NB-180-P	6.2	28.4	19.0	30.0	7300
TiO <sub>2</sub> NB-220-P	6.0	23.6	15.1	29.5	8100
TiO <sub>2</sub> NB-500-P	7.1	28.9	19.6	27.2	5980
Planar TiO <sub>2</sub> -P	7.1	38.3	22.7	42.5	5680

<sup>a</sup>The PL lifetimes ( $\tau_1$ ,  $\tau_2$ , and  $\tau$ ) are fitted by the biexponential model:  $y = A_1 \cdot \exp(x/\tau_1) + A_2 \cdot \exp(x/\tau_2)$ ,  $A_1$  and  $A_2$  are the prefactors,  $\tau_1$  and  $\tau_2$  are the lifetimes of the fast and slow decay component, respectively, and  $\tau = A_1/(A_1+A_2) \cdot \tau_1 + A_2/(A_1+A_2) \cdot \tau_2$ .

To gain a deeper insight into the photovoltaic performance improvement by TiO<sub>2</sub> NB structures, we resorted to electrochemical impedance spectroscopy (EIS) characterization, which is a powerful technique for investigating the mechanism of carrier transport and recombination in solar cells.<sup>80</sup> The Nyquist plots for different TiO<sub>2</sub> structures based C-PSCs measured under dark at a bias voltage of 0.8 V are presented in Figure 6b and c. The equivalent circuit shown in the inset of Figure 6b was used for fitting the EIS data and the detailed fitting result is summarized in Table 2. The large semicircle in the low-frequency range was attributed to recombination resistance ( $R_{rec}$ ) and capacitance in literature reports, and a higher  $R_{rec}$  is associated with a lower carrier recombination.<sup>40</sup> As shown in Figure 6b, for the cells,  $R_{rec}$  follows the sequence of TiO<sub>2</sub> NB-220-P > TiO<sub>2</sub> NB-180-P > TiO<sub>2</sub> NB-500-P > Planar TiO<sub>2</sub>-P, highlighting the role of TiO<sub>2</sub> NB arrays in abating the carrier recombination. Conceivably, the porous structure of TiO<sub>2</sub> NB arrays would increase the interface area of the perovskite and TiO<sub>2</sub>, meaning that excitons or the resulting charge carriers can more easily drift to the interface for charge separation with reduced occurrence of trap-assisted recombination. It should be noted that the transmission line behaviour is not present in the EIS plot before the recombination RC element as in the conventional dye-sensitized solar cells with the relatively thick TiO<sub>2</sub> film (8-12  $\mu$ m) being the electron pathway.<sup>26,81</sup> This should be mainly due to the much faster electron transport in PSCs resulting from the much thinner meso-layer (800 nm-1.5  $\mu$ m), the two transport pathways (perovskite layer and TiO<sub>2</sub> layer) and the built-in potential for electron drift, which make the transport time too small to be clearly observed by EIS.<sup>40</sup> Another important parameter, which can be obtained from the EIS from the intersection point of semicircle with the real axis on the left side, is the series resistance ( $R_s$ ), which is purportedly affected by the ETL.<sup>80</sup> As shown in Figure 6c, the  $R_s$  values of the cells based on TiO<sub>2</sub> NBs

are much lower than that of the planar TiO<sub>2</sub> based device due to the reduced mean thickness of the TiO<sub>2</sub> NB arrays.<sup>82,83</sup>

Figure 6d plots  $R_{rec}$  of different TiO<sub>2</sub> films based C-PSCs as a function of the applied bias voltage ( $V_{appl}$ ). Notably, the  $R_{rec}$  values measured at different  $V_{appl}$  follow the same sequence as those measured at 0.8 V, further verifying the suppression of charge recombination in the TiO<sub>2</sub> NB based C-PSCs. Of course, as the bias increase, the  $R_{rec}$  monotonically decreases as expected. The distinctive charge recombination suppression characteristics of the TiO<sub>2</sub> NB arrays are advantageous for improving  $V_{oc}$  and FF values of C-PSCs.<sup>27</sup>

### 3. Conclusions

In summary, we have developed a facile PS template method to fabricate monolayer ordered TiO<sub>2</sub> NB arrays with varied pore sizes and thicknesses and demonstrated that the TiO<sub>2</sub> NB arrays can serve as efficient ETL for high performance C-PSCs. We have studied the effect of pore sizes and film thicknesses of the TiO<sub>2</sub> NB arrays on the performance of C-PSCs, and the C-PSC based on the TiO<sub>2</sub> NB-220-P array has achieved highest PCE up to 12.02% with good stability. Through a series of optical characterization, FDTD simulation, TRPL and EIS characterizations, we found that the TiO<sub>2</sub> NB array structure with optimum pore size and thickness can reduce reflection losses and thus effectively enhance the light absorption in the active layer. In addition, the open NB structure enhances the quality of the supported perovskite film and increases the interface area between perovskite and TiO<sub>2</sub>, which are favorable for charge separation at the interface and the subsequent charge transport, effectively reducing the occurrence of trap-assisted recombination. Taken together, the results establish the TiO<sub>2</sub> NB arrays as a promising perovskite host for enhancing light absorption and charge separation/transport, and as a platform for understanding the structure-dependent-performance of C-PSCs in depth.

### Acknowledgements

This work was supported by the HK Innovation and Technology Fund (ITS/004/14), the NSFC/HK-RGC Joint Research Scheme (N\_HKUST 610/14) and the Research Grants Council of Hong Kong (AoE/P-02/12).

### Notes

The authors declare no competing financial interest.

### References

1. A. Kojima, K. Teshima, Y. Shirai and T. Miyasaka, *J. Am. Chem. Soc.*, 2009, **131**, 6050-6051.
2. H. S. Kim, C. R. Lee, J. H. Im, K. B. Lee, T. Moehl, A. Marchioro, S. J. Moon, R. Humphry-Baker, J. H. Yum, J. E. Moser, M. Gratzel and N. G. Park, *Sci Rep-Uk*, 2012, **2**, 591.
3. M. Z. Liu, M. B. Johnston and H. J. Snaith, *Nature*, 2013, **501**, 395-398.
4. H. P. Zhou, Q. Chen, G. Li, S. Luo, T. B. Song, H. S. Duan, Z. R.

- Hong, J. B. You, Y. S. Liu and Y. Yang, *Science*, 2014, **345**, 542-546.
5. D. Y. Liu and T. L. Kelly, *Nat. Photonics*, 2014, **8**, 133-138.
  6. S. D. Stranks, G. E. Eperon, G. Grancini, C. Menelaou, M. J. P. Alcocer, T. Leijtens, L. M. Herz, A. Petrozza and H. J. Snaith, *Science*, 2013, **342**, 341-344.
  7. Q. F. Dong, Y. J. Fang, Y. C. Shao, P. Mulligan, J. Qiu, L. Cao and J. S. Huang, *Science*, 2015, **347**, 967-970.
  8. G. C. Xing, N. Mathews, S. Y. Sun, S. S. Lim, Y. M. Lam, M. Gratzel, S. Mhaisalkar and T. C. Sum, *Science*, 2013, **342**, 344-347.
  9. W. S. Yang, J. H. Noh, N. J. Jeon, Y. C. Kim, S. Ryu, J. Seo and S. I. Seok, *Science*, 2015, **348**, 1234-1237.
  10. M. M. Lee, J. Teuscher, T. Miyasaka, T. N. Murakami and H. J. Snaith, *Science*, 2012, **338**, 643-647.
  11. L. Etgar, P. Gao, Z. S. Xue, Q. Peng, A. K. Chandiran, B. Liu, M. K. Nazeeruddin and M. Gratzel, *J. Am. Chem. Soc.*, 2012, **134**, 17396-17399.
  12. J. J. Shi, J. Dong, S. T. Lv, Y. Z. Xu, L. F. Zhu, J. Y. Xiao, X. Xu, H. J. Wu, D. M. Li, Y. H. Luo and Q. B. Meng, *Appl. Phys. Lett.*, 2014, **104**, 063901.
  13. A. Y. Mei, X. Li, L. F. Liu, Z. L. Ku, T. F. Liu, Y. G. Rong, M. Xu, M. Hu, J. Z. Chen, Y. Yang, M. Gratzel and H. W. Han, *Science*, 2014, **345**, 295-298.
  14. Z. H. Wei, K. Y. Yan, H. N. Chen, Y. Yi, T. Zhang, X. Long, J. K. Li, L. X. Zhang, J. N. Wang and S. H. Yang, *Energ. Environ. Sci.*, 2014, **7**, 3326-3333.
  15. Y. Y. Yang, J. Y. Xiao, H. Y. Wei, L. F. Zhu, D. M. Li, Y. H. Luo, H. J. Wu and Q. B. Meng, *Rsc Adv.*, 2014, **4**, 52825-52830.
  16. S. N. Habisreutinger, T. Leijtens, G. E. Eperon, S. D. Stranks, R. J. Nicholas and H. J. Snaith, *Nano Lett.*, 2014, **14**, 5561-5568.
  17. Z. H. Wei, X. L. Zheng, H. N. Chen, X. Long, Z. L. Wang and S. H. Yang, *J. Mater. Chem. A*, 2015, **3**, 16430-16434.
  18. H. W. Zhou, Y. T. Shi, Q. S. Dong, H. Zhang, Y. J. Xing, K. Wang, Y. Du and T. L. Ma, *J. Phys. Chem. Lett.*, 2014, **5**, 3241-3246.
  19. X. Li, M. Tschumi, H. W. Han, S. S. Babkair, R. A. Alzubaydi, A. A. Ansari, S. S. Habib, M. K. Nazeeruddin, S. M. Zakeeruddin and M. Gratzel, *Energy Technol.-Ger.*, 2015, **3**, 551-555.
  20. K. Leo, *Nat. Nanotechnol.*, 2015, **10**, 574-575.
  21. G. D. Niu, X. D. Guo and L. D. Wang, *J. Mater. Chem. A*, 2015, **3**, 8970-8980.
  22. K. C. Wang, J. Y. Jeng, P. S. Shen, Y. C. Chang, E. W. G. Diau, C. H. Tsai, T. Y. Chao, H. C. Hsu, P. Y. Lin, P. Chen, T. F. Guo and T. C. Wen, *Sci Rep-Uk*, 2014, **4**, 4756.
  23. Z. G. Xiao, C. Bi, Y. C. Shao, Q. F. Dong, Q. Wang, Y. B. Yuan, C. G. Wang, Y. L. Gao and J. S. Huang, *Energ. Environ. Sci.*, 2014, **7**, 2619-2623.
  24. Q. Wang, Y. C. Shao, Q. F. Dong, Z. G. Xiao, Y. B. Yuan and J. S. Huang, *Energ. Environ. Sci.*, 2014, **7**, 2359-2365.
  25. F. Hao, C. C. Stoumpos, Z. Liu, R. P. H. Chang and M. G. Kanatzidis, *J. Am. Chem. Soc.*, 2014, **136**, 16411-16419.
  26. X. B. Xu, Z. H. Liu, Z. X. Zuo, M. Zhang, Z. X. Zhao, Y. Shen, H. P. Zhou, Q. Chen, Y. Yang and M. K. Wang, *Nano Lett.*, 2015, **15**, 2402-2408.
  27. Z. H. Wei, H. N. Chen, K. Y. Yan and S. H. Yang, *Angew Chem Int Edit*, 2014, **53**, 13239-13243.
  28. F. Q. Zhang, X. C. Yang, H. X. Wang, M. Cheng, J. H. Zhao and L. C. Sun, *Acs Appl. Mater. Inter.*, 2014, **6**, 16140-16146.
  29. Z. Li, S. A. Kulkarni, P. P. Boix, E. Z. Shi, A. Y. Cao, K. W. Fu, S. K. Batabyal, J. Zhang, Q. H. Xiong, L. H. Wong, N. Mathews and S. G. Mhaisalkar, *Acs Nano*, 2014, **8**, 6797-6804.
  30. J. Cao, Y. M. Liu, X. J. Xiao, J. Yin, J. Li, B. Xu, Y. Z. Tan and N. F. Zheng, *J. Am. Chem. Soc.*, 2015, **137**, 10914-10917.
  31. K. Y. Yan, Z. H. Wei, J. K. Li, H. N. Chen, Y. Yi, X. L. Zheng, X. Long, Z. L. Wang, J. N. Wang, J. B. Xu and S. H. Yang, *Small*, 2015, **11**, 2269-2274.
  32. Z. W. Wu, S. Bai, J. Xiang, Z. C. Yuan, Y. G. Yang, W. Cui, X. Y. Gao, Z. Liu, Y. Z. Jin and B. Q. Sun, *Nanoscale*, 2014, **6**, 10505-10510.
  33. M. Batmunkh, C. J. Shearer, M. J. Biggs and J. G. Shapter, *J. Mater. Chem. A*, 2015, **3**, 9020-9031.
  34. H. Chen, Z. Wei, X. Zheng and S. Yang, *Nano Energy*, 2015, **15**, 216-226.
  35. M. Hu, L. F. Liu, A. Y. Mei, Y. Yang, T. F. Liu and H. W. Han, *J. Mater. Chem. A*, 2014, **2**, 17115-17121.
  36. K. Cao, J. Cui, H. Zhang, H. Li, J. K. Song, Y. Shen, Y. B. Cheng and M. K. Wang, *J. Mater. Chem. A*, 2015, **3**, 9116-9122.
  37. X. Y. Wang, Z. Li, W. J. Xu, S. A. Kulkarni, S. K. Batabyal, S. Zhang, A. Y. Cao and L. H. Wong, *Nano Energy*, 2015, **11**, 728-735.
  40. W. J. Ke, G. J. Fang, Q. Liu, L. B. Xiong, P. L. Qin, H. Tao, J. Wang, H. W. Lei, B. R. Li, J. W. Wan, G. Yang and Y. F. Yan, *J. Am. Chem. Soc.*, 2015, **137**, 6730-6733.
  41. H. H. Wang, Q. Chen, H. P. Zhou, L. Song, Z. St Louis, N. De Marco, Y. H. Fang, P. Y. Sun, T. B. Song, H. J. Chen and Y. Yang, *J. Mater. Chem. A*, 2015, **3**, 9108-9115.
  42. N. J. Jeon, J. H. Noh, Y. C. Kim, W. S. Yang, S. Ryu and S. Il Seol, *Nat. Mater.*, 2014, **13**, 897-903.
  43. E. Edri, S. Kirmayer, A. Henning, S. Mukhopadhyay, K. Gartsman, Y. Rosenwaks, G. Hodes and D. Cahen, *Nano Lett.*, 2014, **14**, 1000-1004.
  44. T. Salim, S. Y. Sun, Y. Abe, A. Krishna, A. C. Grimsdale and Y. M. Lam, *J. Mater. Chem. A*, 2015, **3**, 8943-8969.
  45. S. Aharon, S. Gamliel, B. El Cohen and L. Etgar, *Phys. Chem. Chem. Phys.*, 2014, **16**, 10512-10518.
  46. Y. X. Zhao, A. M. Nardes and K. Zhu, *J. Phys. Chem. Lett.*, 2014, **5**, 490-494.
  47. T. Leijtens, B. Lauber, G. E. Eperon, S. D. Stranks and H. J. Snaith, *J. Phys. Chem. Lett.*, 2014, **5**, 1096-1102.
  48. M. T. Horantner, W. Zhang, M. Saliba, K. Wojciechowski and H. J. Snaith, *Energ. Environ. Sci.*, 2015, **8**, 2041-2047.
  49. Y. Li, X. Z. Ye, Y. R. Ma and L. M. Qi, *Small*, 2015, **11**, 1183-1188.
  50. S. Y. Chen, Y. T. Yen, Y. Y. Chen, C. S. Hsu, Y. L. Chueh and L. J. Chen, *Rsc Adv.*, 2012, **2**, 1314-1317.
  51. P. Q. Gao, H. Z. Wang, Z. X. Sun, W. Q. Han, J. S. Li and J. C. Ye, *Appl. Phys. Lett.*, 2013, **103**, 253105.
  52. S. H. Zhong, Z. G. Huang, X. X. Lin, Y. Zeng, Y. C. Ma and W. Z. Shen, *Adv. Mater.*, 2015, **27**, 555-561.
  53. Y. C. Qiu, S. F. Leung, Q. P. Zhang, C. Mu, B. Hua, H. Yan, S. H. Yang and Z. Y. Fan, *Sci. Bull.*, 2015, **60**, 109-115.
  54. S. Deki, Y. Aoi, Y. Asaoka, A. Kajinami and M. Mizuhata, *J. Mater. Chem.*, 1997, **7**, 733-736.
  55. H. N. Chen, Z. H. Wei, K. Y. Yan, Y. Yi, J. N. Wang and S. H. Yang, *Faraday Discuss.*, 2014, **176**, 271-286.
  56. C.-G. Wu, C.-H. Chiang, Z.-L. Tseng, M. K. Nazeeruddin, A. Hagfeldt and M. Gratzel, *Energy Environ. Sci.*, 2015, **8**, 2725-2733.
  57. Y. H. Yu, J. Y. Li, D. L. Geng, J. L. Wang, L. S. Zhang, T. L. Andrew, M. S. Arnold and X. D. Wang, *Acs Nano*, 2015, **9**, 564-572.
  58. D. W. deQuilettes, S. M. Vorpahl, S. D. Stranks, H. Nagaoka, G. E. Eperon, M. E. Ziffer, H. J. Snaith and D. S. Ginger, *Science*, 2015, **348**, 683-686.
  59. W. Y. Nie, H. H. Tsai, R. Asadpour, J. C. Blancon, A. J. Neukirch, G. Gupta, J. J. Crochet, M. Chhowalla, S. Tretiak, M. A. Alam, H. L. Wang and A. D. Mohite, *Science*, 2015, **347**, 522-525.
  60. J. Burschka, N. Pellet, S. J. Moon, R. Humphry-Baker, P. Gao, M. K. Nazeeruddin and M. Gratzel, *Nature*, 2013, **499**, 316-319.
  61. D. Y. Liu, M. K. Gangishetty and T. L. Kelly, *J. Mater. Chem. A*, 2014, **2**, 19873-19881.
  62. H. J. Snaith, A. Abate, J. M. Ball, G. E. Eperon, T. Leijtens, N. K. Noel, S. D. Stranks, J. T. W. Wang, K. Wojciechowski and W. Zhang, *J. Phys. Chem. Lett.*, 2014, **5**, 1511-1515.
  63. J. D. Chen, C. H. Cui, Y. Q. Li, L. Zhou, Q. D. Ou, C. Li, Y. F. Li and

- J. X. Tang, *Adv. Mater.*, 2015, **27**, 1035-1041.
64. H. Y. Wei, J. H. Huang, C. Y. Hsu, F. C. Chang, K. C. Ho and C. W. Chu, *Energ. Environ. Sci.*, 2013, **6**, 1192-1198.
65. H. K. Raut, V. A. Ganesh, A. S. Nair and S. Ramakrishna, *Energ. Environ. Sci.*, 2011, **4**, 3779-3804.
66. J. G. Cai and L. M. Qi, *Mater. Horizons*, 2015, **2**, 37-53.
67. S. J. Ha and J. H. Moon, *Sci Rep-Uk*, 2014, **4**, 5375.
68. S. F. Leung, Q. P. Zhang, F. Xiu, D. L. Yu, J. C. Ho, D. D. Li and Z. Y. Fan, *J. Phys. Chem. Lett.*, 2014, **5**, 1479-1495.
69. Q. F. Lin, S. F. Leung, L. F. Lu, X. Y. Chen, Z. Chen, H. N. Tang, W. J. Su, D. D. Li and Z. Y. Fan, *Acs Nano*, 2014, **8**, 6484-6490.
70. P. Loper, M. Stuckelberger, B. Niesen, J. Werner, M. Filipic, S. J. Moon, J. H. Yum, M. Topic, S. De Wolf and C. Ballif, *J. Phys. Chem. Lett.*, 2015, **6**, 66-71.
71. L. A. Fielding, O. O. Mykhaylyk, A. Schmid, D. Pontoni, S. P. Armes and P. W. Fowler, *Chem. Mater.*, 2014, **26**, 1270-1277.
72. J. Ferber and J. Luther, *Sol. Energ. Mat. Sol. C.*, 1998, **54**, 265-275.
73. C. Cheng, M. M. Lee, N. K. Noel, G. M. Hughes, J. M. Ball, H. E. Assender, H. J. Snaith and A. A. R. Watt, *Acs Appl. Mater. Inter.*, 2014, **6**, 14247-14252.
74. S. Hore, P. Nitz, C. Vetter, C. Prah, M. Niggemann and R. Kern, *Chem Commun*, 2005, 2011-2013.
75. J. W. Lee, J. Lee, C. Kim, C. Y. Cho and J. H. Moon, *Sci Rep-Uk*, 2014, **4**, 6804.
76. X. Chen, S. Yang, Y. C. Zheng, Y. Chen, Y. Hou, X. H. Yang and H. G. Yang, *Adv. Sci.*, 2015, **2**, DOI: 10.1002/advs.201500105.
77. A. Listorti, E. J. Juarez-Perez, C. Frontera, V. Roiati, L. Garcia-Andrade, S. Colella, A. Rizzo, P. Ortiz and I. Mora-Sero, *J. Phys. Chem. Lett.*, 2015, **6**, 1628-1637.
78. D. Shi, V. Adinolfi, R. Comin, M. J. Yuan, E. Alarousu, A. Buin, Y. Chen, S. Hoogland, A. Rothenberger, K. Katsiev, Y. Losovyj, X. Zhang, P. A. Dowben, O. F. Mohammed, E. H. Sargent and O. M. Bakr, *Science*, 2015, **347**, 519-522.
79. W. Zhang, M. Saliba, S. D. Stranks, Y. Sun, X. Shi, U. Wiesner and H. J. Snaith, *Nano Lett.*, 2013, **13**, 4505-4510.
80. K. Wang, Y. T. Shi, Q. S. Dong, Y. Li, S. F. Wang, X. F. Yu, M. Y. Wu and T. L. Ma, *J. Phys. Chem. Lett.*, 2015, **6**, 755-759.
81. V. Gonzalez-Pedro, E. J. Juarez-Perez, W.-S. Arsyad, E. M. Barea, F. Fabregat-Santiago, I. Mora-Sero, and J. Bisquert, *Nano Lett.* 2014, **14**, 888-893
82. P. Tiwana, P. Docampo, M. B. Johnston, H. J. Snaith and L. M. Herz, *Acs Nano*, 2011, **5**, 5158-5166.
83. A. K. Chandiran, M. Abdi-Jalebi, M. K. Nazeeruddin and M. Gratzel, *Acs Nano*, 2014, **8**, 2261-2268.